Petroleum Science 20 (2023) 1922–1933

Contents lists available at ScienceDirect

Petroleum Science

journal homepage: www.keaipublishing.com/en/journals/petroleum-science

Original Paper

Active precursor promoting nucleation/growth of MWW zeolite and controlling its morphology

Shi-Wei Cao [a, c, 1], Peng Xiao [a, 1], Jie Wang [a], Yu Sun [a], Yun-Shan Shang [a], Ya-Fen Ge [a], Qi Liu [a], Yan-Jun Gong [a, *], Guang Mo [b], Zhi-Hong Li [b, **]

[a] State Key Laboratory of Heavy Oil Processing, Key Laboratory of Catalysis of CNPC, China University of Petroleum-Beijing, Beijing 102249, China
[b] Beijing Synchrotron Radiation Facility, Institute of High Energy Physics, Chinese Academy of Sciences, Beijing 100039, China
[c] Cangzhou Risun Chemical Co. Ltd., Hebei 061000, China

ARTICLE INFO

Article history:
Received 18 April 2022
Received in revised form
9 October 2022
Accepted 5 January 2023
Available online 9 January 2023

Edited by Jia-Jia Fei

Keywords:
MWW zeolites
Active precursor
Small-angle X-ray scattering
Benzene-ethylene alkylation reaction

ABSTRACT

MWW zeolites is an important catalyst in petrochemical industry. However, the efficient preparation of MWW zeolites still faces challenges, and the origin of influential factors for regulating its structure properties also remains obscure. Herein, we designed a nanoscale amorphous silica-alumina species denoted as active precursor (APS), and adopt the APS in the HMI mixture to synthesize MCM-22 zeolite (APS-MWW) successfully. To reveal the distinctive role of APS in promoting the crystallization of MWW zeolites, two crystal materials (ITQ-1 and MCM-22) and one mother liquor (ML) as seeds to synthesize three types of MWW zeolites. Typically, when adding APS in the synthetic mixture, the HMI amount was reduced to less than a quarter and crystallization time was reduced to 36 h. APS-MWW sample provides a smaller particle size (2–4 μm) and thinner stacked layer thickness (5–20 nm). Synchrotron radiation Small Angle X-ray Scattering (SAXS) shows each seed has a different impact on the species' fractal structure and size distribution in the mixture, which is highly related to the nucleation and growth of MWW zeolites. APS shows a large number of 6 membered ring (MR) structure units which play a significant role in boosting the rapid nucleation and growth of APS-MWW zeolite. Among the synthesized MWW zeolites, the APS-MWW performs the highest ethylbenzene yield in the alkylation reaction of benzene-ethylene, which is attributed to its moderate flake thickness, appropriate texture properties and more external surface acidity. The results will provide a new perspective for producing MWW-types zeolites by using the available and effective active precursor.
© 2023 The Authors. Publishing services by Elsevier B.V. on behalf of KeAi Communications Co. Ltd. This is an open access article under the CC BY-NC-ND license (http://creativecommons.org/licenses/by-nc-nd/4.0/).

1. Introduction

Ethylbenzene (EB) is an important intermediate in the petrochemical industry, primarily produced from the alkylation of benzene, which mainly used for dehydrogenation to produce styrene monomer, and then to synthesize and produce polystyrene, expanded polystyrene, styrene butadiene rubber and styrene butadiene latex, and other polymer materials (Zhang et al., 2012; Yang et al., 2016). For improving ethylbenzene yield, the efficient catalyst is still the key to satisfy the sustainable development. Currently, MWW zeolites catalyst can provide an effective breakthrough in the enhancement of EB selectivity under the condition of low benzene/ethylene molar ratio at low energy output and perform long reaction life (Corma et al., 2000a, b, c; Ebrahimi et al., 2011; Khlebnikova et al., 2017). Typically, MWW zeolites shows the 2D layered structure, possessing two independent pore systems: i) the 2D sinusoidal 10 membered ring (MR) channels, ii) 12 MR and hemi-supercages (pockets) distributed on the surface, which endows excellent catalytic properties in multiple reactions i.e. cracking, isomerization, alkylation, hydroisomerization, dehydration, and aromatization (Corma et al., 1996, 2000; Aguilar et al., 2008; Maheshwari et al., 2010; Carriç;o et al., 2016). Corma et al. (2000b) successfully prepared the ITQ-2 zeolite with a large external surface area (about 700 $m^2 \cdot g^{-1}$) by swelling and delamination on MCM-22-P precursor. Luo et al. (2015) directly synthesized MWW zeolite via using quaternary ammonium salt as organic

* Corresponding author.
** Corresponding author.
E-mail addresses: gongyj@cup.edu.cn (Y.-J. Gong), lzh@ihep.ac.cn (Z.-H. Li).
[1] These authors contributed equally to this research work.

https://doi.org/10.1016/j.petsci.2023.01.005
1995-8226/© 2023 The Authors. Publishing services by Elsevier B.V. on behalf of KeAi Communications Co. Ltd. This is an open access article under the CC BY-NC-ND license (http://creativecommons.org/licenses/by-nc-nd/4.0/).

structure-directing agents (OSDAs), compared with the traditional MCM-56, the external surface area of MIT-1 zeolite is more than 500 $m^2 \cdot g^{-1}$. Margarit et al. (2015) synthesized DS-ITQ-2 zeolite with monolayer structure directly by using double template, compared with post-treated ITQ-2, DS-ITQ-2 shows higher hydrothermal stability, the single and double layers are about 70% and the external surface area is more than 300 $m^2 \cdot g^{-1}$. The extensive researches show that the acid sites on the exterior surface of MWW zeolite are more active than that on the inner cavity in the alkylation reaction of benzene with ethylene to produce EB (Du and Olson, 2002; Liu et al., 2011). Therefore, designing feasible process to fabricate MWW zeolites with controllable structure and at low fabrication cost is highly desirable.

As known, involvement of zeolite seeds can enhance the crystallization rate of zeolites and adjust its morphological structure, and also reduce dosage of OSDAs or without using OSDAs (Díaz et al., 2006; Kamimura et al., 2017; Rodrigues et al., 2018). Kamimura et al. (2017) obtained MCM-49 zeolite using MCM-22 as the seeds and the results showed that the crystallization time was shortened, but the MOR crystal phase appeared. By using MCM-22, the delayered MCM-22 and ITQ-2 as seeds for synthesizing MWW zeolites, respectively, Díaz et al. (2006) found the delaminated ITQ-2 seeds, due to its more surface defects, could produce more nuclei and finally resulted in the high crystallinity and smaller size MWW zeolites. However, if using the larger crystal as seeds, the resultant zeolite crystal goes bigger in size and the synthesis efficiency is worse. Rodrigues et al. (2018) synthesized MCM-22 zeolite by using the three types of MCM-22 seeds, i.e. common MCM-22, ball milled MCM-22 and the micro-seeds in the mother liquor, they pointed out, the ball milled seeds mixture could produce the final zeolite at shorter crystallization time and the average crystal size was reduced from 29 to 3.5 μm. Recently, a “seeding gel”, which was obtained at the end of the induction period of MWW zeolites crystallization process, was used in the synthesis of MWW zeolites (Shi et al., 2015). This “seeding gel” material bears some structural similarities to the target zeolite, but not a long-range periodic structure, thus, synthesis of MWW zeolites need combination of HMI with the phenylamine (AN) as structure-promoting agents. However, the synthesized MWW zeolites performs no much improvement in selectivity of ethylbenzene in the reaction of liquid-phase alkylation of benzene with ethylene.

As reported, some X-ray amorphous zeolitic materials (considered as zeolite embryos or zeolite precursors) have greatly attracted the attention of researchers. Spectroscopic characterizations demonstrated that these materials possess zeolitic acidity, large external surface area and enhanced accessibility of active sites, leading to improved catalytic performance (Inagaki et al., 2014; Haw et al., 2018; Bai et al., 2020). This type of material features an amorphous structure but possesses a large number of structural units, which can effectively promote the nucleation and crystallization of zeolites (Sheng et al., 2021; Wang et al., 2021). This will inspire to optimize zeolite synthesis process, improve MWW zeolite properties, thus further enhance the performance of the alkylation reaction.

Small Angle X-ray Scattering (SAXS) technique has been established to study zeolite synthesis mechanism, owing to its powerful nondestructive testing function for determining the evolution of precursor during crystallization process. With the aid of SAXS, Fan et al. (2007) emphasized that three kinds of particles (primary unit, precursor particle, and nanosized LTA) played a significant role in the crystallization of LTA zeolite. Tompsett et al. (2007) studied the synthesis process of Y zeolite in the microwave by using SAXS, and revealed the reorganization of precursors generate crystal nuclei. Hould et al. (2008, 2010, 2011) showed that template TEA^+ facilitates to nucleation, Na^+ shortens nucleation rates and improves crystallization rates in growth system of Beta zeolite. In our previous work, by determining the evolution of silica-alumina species in the sol precursor for synthesis of NaY zeolite, we (Zhao et al., 2017) found fractal structure of species can be a valuable criterion as an active precursor, corresponding to its suitable size and compactness for generating a highly crystalline NaY zeolite. Schwanke et al. (2020) devoted to study the growth process of the MWW lamellar precursors by SAXS, indicated the presence of primary nanoparticles population at the initial crystallization stage, benefit to their growth and transformation from spherical nanoparticles to lamellar precursor. However, the essential for regulating the structural morphology in zeolite synthesis still remains obscure.

In this work, using an active precursor (APS), combined with other three types of seeds (ITQ-1, MCM-22 and ML) in the MWW zeolites synthesis system, APS-MWW, ITQ-MWW, ML-MWW and MCM-MWW samples were obtained respectively and systematically characterized. All of these seeds play an important role in reducing crystal size, stacked layer thickness and the amount of OSDAs, and meanwhile reducing the crystallization time. Comparatively, APS features a long-range disordered amorphous material containing a large number of 6 MR structures, leading to rapid nucleation during the induction period, and boosting APS-MWW rapid growth, which results in very short crystallization time (36 h), that it would take 120 h with traditional method. Notably, for APS material synthetic system, the evolution behavior of the precursor in the aging process was determined by using SAXS and other techniques. The results show that the APS possesses a large number of 6 MR structural units in the early aging process, which improve crystal nucleation, zeolite growth, which should account for the highly effective formation of APS-MWW zeolites. This provides important guidance for the efficient and low-cost synthesis of MWW zeolites. In addition, the efficient preparation of zeolites is of great significance to the green and sustainable development of petrochemical industry.

2. Experimental section

2.1. Preparation of APS

APS was synthesized using silica (Qingdao Haiyang Chemical Company), sodium hydroxide (NaOH, 99 wt%, A.R. Beijing Chemical Company), $NaAlO_2$ (Al_2O_3, 45 wt%; Na_2O, 27 wt%, A.R. Sinopharm Chemical Reagent Co), HMI (hexamethyleneimine > 98 wt%, A.R. Sigma-Aldrich) and deionized water. The final gel (SiO_2: 0.10 Na_2O: (0–0.033) Al_2O_3: 0.1 HMI: 20 H_2O) was heated at 150 °C for an appointed time before its initial crystallization stage and the final product obtained after filtrating, washing, drying at 100 °C. The ultimate product was amorphous, designated as APS. The syntheses for other seeds (ITQ-1, MCM-22 and ML) are shown in the Supporting Information (1.1, 1.2 and 1.3). ITQ-1 and MCM-22 seeds are well-structured zeolites and the mother liquid (ML) was collected by the filtration in the MCM-22 synthesis.

2.2. Preparation of MWW zeolite

The MCM-22 zeolite was prepared with the molar ratio SiO_2: 0.05 Na_2O: 0.033 Al_2O_3: 0.1 HMI: 10–25 H_2O: 0.05–0.15 APS. All reactants were mixed to obtain a gel. After stirring for 6 h, the aged clear synthesis solution was transferred into a Teflon lined stainless steel autoclave and hydrothermally treated at 150 °C for 36 h under rotation condition (60 rpm). The MWW product named as APS-MWW (Run 2, Table S1) was collected by filtrating, washing, drying at 100 °C. Herein, the corresponding samples prepared were denoted as X-MWW-P, where X refers the type of seeds and P refers

to the MWW zeolites precursor. To prepare the H-form-product (APS-MWW), APS-MWW-P was stirred with 1 M NH_4Cl solution at 90 °C for 2 h twice and then calcined at 550 °C. For the synthesis of other types of MWW zeolites, ML-MWW-P (Run 3, Table S1), ITQ-MWW-P (Run 4, Table S1) and MCM-MWW-P (Run 5, Table S1), the same method was used, and just ML, ITQ-1 and MCM-22 zeolite as seeds, denoted as ITQ-MWW, ML-MWW and MCM-MWW, respectively. For comparison, traditional MCM-22 samples (noted as MCM-22-P) were synthesized (Run 1, Table S1) similar to a previously reported in the literature (Corma et al., 1995a, b).

Adopting APS, the MWW family members (MCM-22, MCM-49 and MCM-56) could be achieved by varying the synthetic parameters. Fig. 1 gives the phase diagram for synthesis MWW using APS and intuitively displays the alkaline concentration (OH^-/SiO_2 ratio), Al content (SiO_2/Al_2O_3), H_2O content (H_2O/SiO_2), HMI content (HMI/SiO_2), APS content and crystallization time. A lower alkalinity ($OH^-/SiO_2 \leq 0.1$), higher SiO_2/Al_2O_3 ratio ($SiO_2/Al_2O_3 = 25–120$) and APS content (5%–15%) facilitates to obtain the MCM-22 precursor. Conversely, as alkalinity ($OH^-/SiO_2 = 0.1–0.5$) and APS content (15%–60%) enhance, SiO_2/Al_2O_3 decreases ($SiO_2/Al_2O_3 = 25–40$), MCM-49 zeolite can be acquired. MCM-56 zeolite as a transient state (crystallization time with 18–24 h) has a narrow phase with lower amount of HMI ($HMI/SiO_2 \leq 0.05$) and APS content (< 5%). Comprehensive evaluation, MCM-22 zeolite has a relatively wide phase and an energy-efficient synthetic process which makes it to be more suitable for large scale production in industrial environment.

3. Results and discussion

3.1. Synthesis and characterization of MWW zeolites

All as-synthesized MWW zeolites obtained by using APS, ML, ITQ-1 and MCM-22 as seeds, respectively, have well-structured MCM-22-P characteristics (Fig. 2a), indicating that the seeds work effectively (Corma et al., 1995a, b). The crystallization curves (Fig. 2b) show that the APS-MWW-P manifests the highest synthesis efficiency among these five samples. Typically, APS-MWW-P sample presents one third of induction period and crystallization period (12 h and 36 h), compared to conventional MCM-22-P (36 h and 120 h). Though the other seeds can promote synthesis of MCM-22 zeolites but it still needs more than 48 h. Here, APS-MWW-P sample presents the shortest induction and fastest growth period, indicating that the APS should have its special function in promoting the nucleation and growth of MWW zeolites.

APS-MWW-P sample (Fig. 3a and b) presents 2–4 μm microsphere aggregate in diameter composed of small hexagonal flakes with the size length of 200–400 nm and the thickness of 5–20 nm (Fig. 3c). The ML-MWW-P sample (Fig. 3d and e) appears a flake-like particles, of which the edges are twisted, and the thickness of the lamellae is about 2.5–10 nm (Fig. 3f). Compared with APS-MWW-P sample, the ITQ-MWW-P sample (Fig. 3g and h) presents stacking aggregate by the larger flake (400–600 nm) with the curved edges, and thickness of 5–15 nm (Fig. 3i). The MCM-MWW-P sample (Fig. 3j and k) shows randomly dispersed larger hexagonal flakes, which may be caused by epitaxial growth. The flake thickness is in the range of 20–50 nm (Fig. 3l) similar to the samples synthesized by conventional methods. In summary, the addition of seeds significantly affects the morphology and thickness of MWW zeolites. Peculiarly, the APS-MWW-P sample has a smaller size of hexagonal flakes (200–400 nm) and moderate flake thickness (5–20 nm) among these four samples, which is beneficial to the alkylation reaction in industrial application.

N_2 adsorption-desorption analysis (Fig. 4) shows that all samples display the existence of intergranular mesopores/macropores formed by the MWW layers with pore distribution of 20–80 nm, due to the accumulation of particles. Notably, APS-MWW sample possesses the largest specific surface area (613 $m^2\ g^{-1}$) and mesopore volume (0.61 $cm^3\ g^{-1}$) as seen in Table 1. The ML-MWW sample has the largest external surface area (163 $m^2\ g^{-1}$) and higher mesopore volume (0.53 $cm^3\ g^{-1}$). ITQ-MWW (S_{BET}: 546 $m^2\ g^{-1}$, V_{mes}: 0.42 $cm^3\ g^{-1}$) and MCM-MWW (S_{BET}: 552 $m^2\ g^{-1}$, V_{mes}: 0.41 $cm^3\ g^{-1}$) have similar texture properties. The different types of seeds have significant influence on the external surface area and pore volume of MWW zeolites. Accordingly, smaller particles size of MWW zeolites is beneficial to increase the external surface area and pore volume, and higher ratio of HMI/SiO_2 is conducive to the formation of MWW zeolite micropores (Haw et al., 2018). Owing to the presence of APS, APS-MWW zeolite can be produced under lower ratio of HMI/SiO_2 and it has a staggered stacking of MWW sheets. A typical example, APS-MWW with $HMI/SiO_2 = 0.1$ gives the external surface area and mesopore volume of 146 $m^2\ g^{-1}$ and 0.61 $cm^3\ g^{-1}$, respectively, while MCM-22 synthesized by the conventional method with HMI/SiO_2 of 0.4 is 66 $m^2\ g^{-1}$ and 0.37 $cm^3\ g^{-1}$, respectively (Cao et al., 2021). The results show that APS is more conducive to the efficient synthesis of MWW zeolite with excellent texture properties, which will lay the foundation for the efficient synthesis of MCM-22 zeolite.

TG/DTG analysis was used to determine the content of OSDAs inside the as-synthesized MWW-P samples when using different

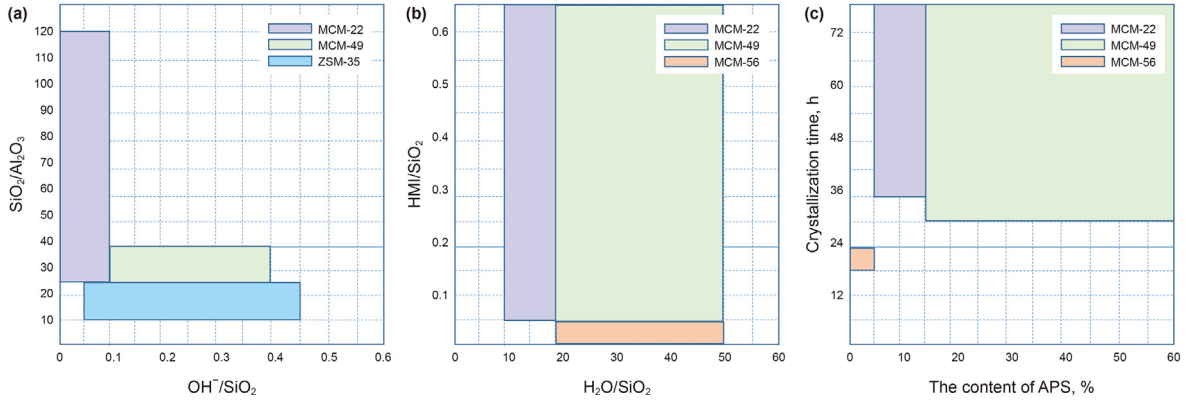

Fig. 1. (**a**) The influence of alkali content and aluminum content on the product ($HMI/SiO_2 = 0.1$, $H_2O/SiO_2 = 15$), (**b**) The influence of H_2O content and HMI content on the product ($SiO_2/Al_2O_3 = 30$, $OH^-/SiO_2 = 0.1$). (**c**) The influence of APS content and crystallization time on the product ($SiO_2/Al_2O_3 = 30$, $OH^-/SiO_2 = 0.1$, $HMI/SiO_2 = 0.1$, $H_2O/SiO_2 = 15$). All samples were heating at 150 °C under 60 rpm

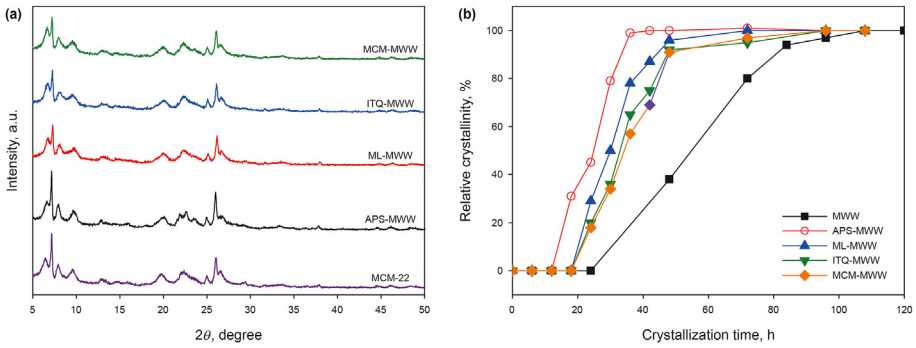

Fig. 2. XRD patterns of (**a**) MWW zeolite precursors, (**b**) crystallization curves of samples.

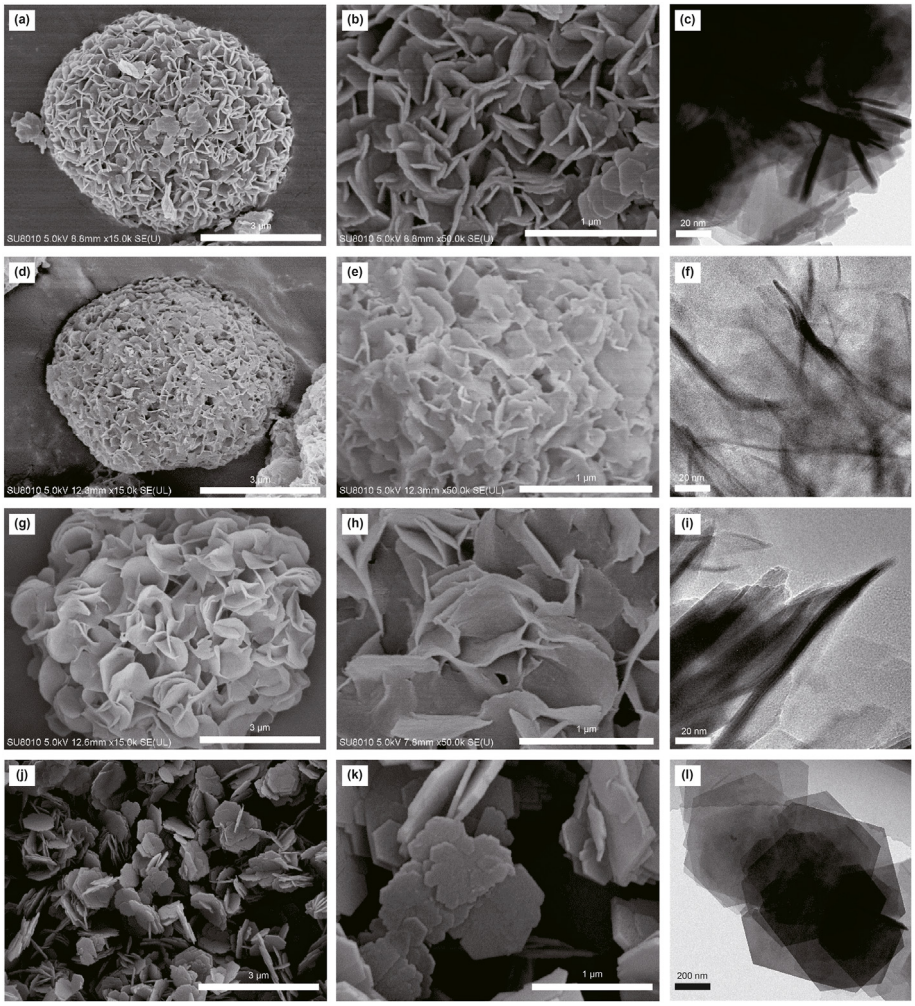

Fig. 3. SEM and TEM images of APS-MWW-P (**a**–**c**), ML-MWW-P (**d**–**f**), ITQ-MWW-P (**g**–**i**) and MCM-MWW-P (**j**–**l**).

seeds. In the TG analysis (Fig. 5), the weight loss between 25 and 200 °C corresponds to the adsorbed water of samples. From 200 °C to 350 °C, all samples give slow and small weight loss which is attributed to the OSDAs molecules located at the 12 MR hemi-cavities between lamellae. According to literature, the fast weight loss between 380 °C and 520 °C should result from oxidation of the OSDAs situated in 10 MR channel (Corma et al., 1995a, b; Jiang et al., 2020). Distinctly, all samples have a smaller interlayer amount of HMI (< 1%) and more 10 MR channel amount of HMI (> 6%) (Table S2). This phenomenon is strongly related to MCM-22 zeolites with higher crystallinity. Among the samples, the APS-MWW has minimum total weight loss. Notably, in the presence of APS, MCM-56 zeolite can be prepared without template (Run 10, Table S1), and the well-crystallized MCM-22 zeolite (Run 6, Table S1) can obtained with HMI/SiO_2 molar ratio as low as 0.05, while FER crystal phase or mixed crystal phase appeared if using other types of seeds (Table S1, Fig. S2). In comparison, the amount of HMI in synthesis of APS-MWW sample (Run 6, Table S1) reduced by 50% or more,

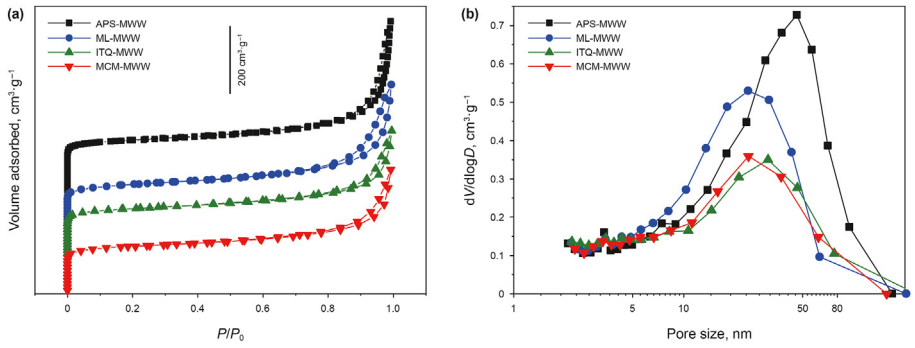

Fig. 4. Texture properties of four samples by using different seeds (**a**) N_2 adsorption/desorption isotherms (The isotherms of APS-MWW, ML-MWW and MCM-MWW were vertically offset by 250 $cm^3\ g^{-1}$,150 $cm^3\ g^{-1}$ and 50 $cm^3\ g^{-1}$, respectively.) and (**b**) pore distribution.

Table 1
Texture properties of as-synthesized samples by using different seeds.

Catalyst	S_{BET}[a], A	S_{mic}, A	S_{ext}, A	V_{tol}, B	V_{mes}, B	V_{mic}[b], B
APS-MWW	613	467	146	0.79	0.61	0.18
ML-MWW	490	327	163	0.66	0.53	0.13
ITQ-MWW	546	410	136	0.58	0.42	0.16
MCM-MWW	552	419	133	0.58	0.41	0.17

[a] BET method.
[b] t-Plot method; A: $m^2 \cdot g^{-1}$; B: $cm^3 \cdot g^{-1}$.

compared to MCM-22 sample with other type of seeds. This indicates that the APS is of evident advantages in the green synthesis of MWW zeolite and ultra-high efficiency.

The SiO_2/Al_2O_3 molar ratio (from XRF measurement) shown in Table S1. The theoretical SiO_2/Al_2O_3 molar ratio in the initial synthesis gel of five samples is 30. All products show a lower SiO_2/Al_2O_3 molar ratio than the theoretical value of gels indicating that some silicon and aluminum species stay in the liquid phase. The final products with SiO_2/Al_2O_3 molar ratio are 27.6 (MCM-22), 22.1 (APS-MWW), 21.3 (ML-MWW), 23.8 (ITQ-MWW) and 25.4 (MCM-MWW), respectively. In a word, seed-assisted synthesis of MWW zeolites promotes the aluminum species into the solid phase, especially, APS and ML can promote more aluminum species into the solid phase system. The solid yields (herein, the solid materials obtained include the crystallized zeolite crystals and amorphous silica-aluminum species) of all samples with different crystallization time had a very similar value (around 90%), but the relative crystallinity was different. Therefore, theoretical yield of the crystal was expressed by relative crystallinity, as shown in Table S3, which is consistent with crystallization curves of samples (Fig. 2b).

The deconvoluted ^{27}Al MAS NMR spectra (Fig. 6) was employed to investigate the effect of seeds on Al localization of four samples and the various Al species distribution was presented in Table S4. The MWW framework contains eight unique tetrahedral sites (T sites) for Al occupancy (Fig. S3). The resonance peak at −2 ppm is often assigned to extra-framework Al (Al^{NF}). The proportion of framework aluminium (Al^F) in APS-MWW (87.3%), ML-MWW (91.0%), ITQ-MWW (85.2%) and MCM-MWW (84.4%) is higher than that of MCM-22 (83.8%). The introduction of seeds promotes the integration of the Al framework, which is beneficial to the stability of MCM-22. Three resonance peaks centered at around 48, 55, and 60 ppm were attributed to the framework tetrahedral aluminum species (Al^F), which were assigned to the Al^F species located in T_6+T_7 (Al^F (48)), T_1+T_3+T_4+T_5+T_8 (Al^F (55)), and T_2 (Al^F (60)) sites (Jiang et al., 2020), respectively. Peak intensity ratios for the three group peaks are 19.5: 41.4: 22.9 (MCM-22), 37.2: 23.5: 26.6 (APS-MWW), 37.4: 23.1: 30.5 (ML-MWW), 24.3: 35.7: 25.2 (ITQ-MWW) and 26.7: 27.0: 30.7 (MCM-MWW), respectively. T_1+T_2+T_3 sites are located in the half cups or supercages, T_4 sites are in the inaccessible parts of the framework. T_6+T_7 sites point to the external surface or in large cavities widely opened on the external surface of crystals and T_5+T_8 sites were assigned to sinusoidal channel systems. APS-MWW and ML-MWW exhibit a bigger portion of Al^F (48) and Al^F (60) than MCM-22, the location of Al species is oriented slightly to the pocket and supercage systems, which may be attributed to that APS-MWW and ML-MWW with smaller crystal size and thinner-layer structure makes more Al species expose to the surface.

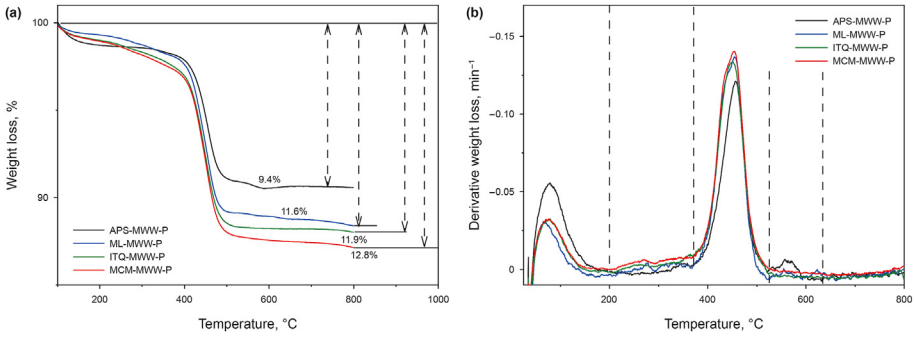

Fig. 5. Four samples by using different seeds of TG (**a**) and DTG (**b**) analysis.

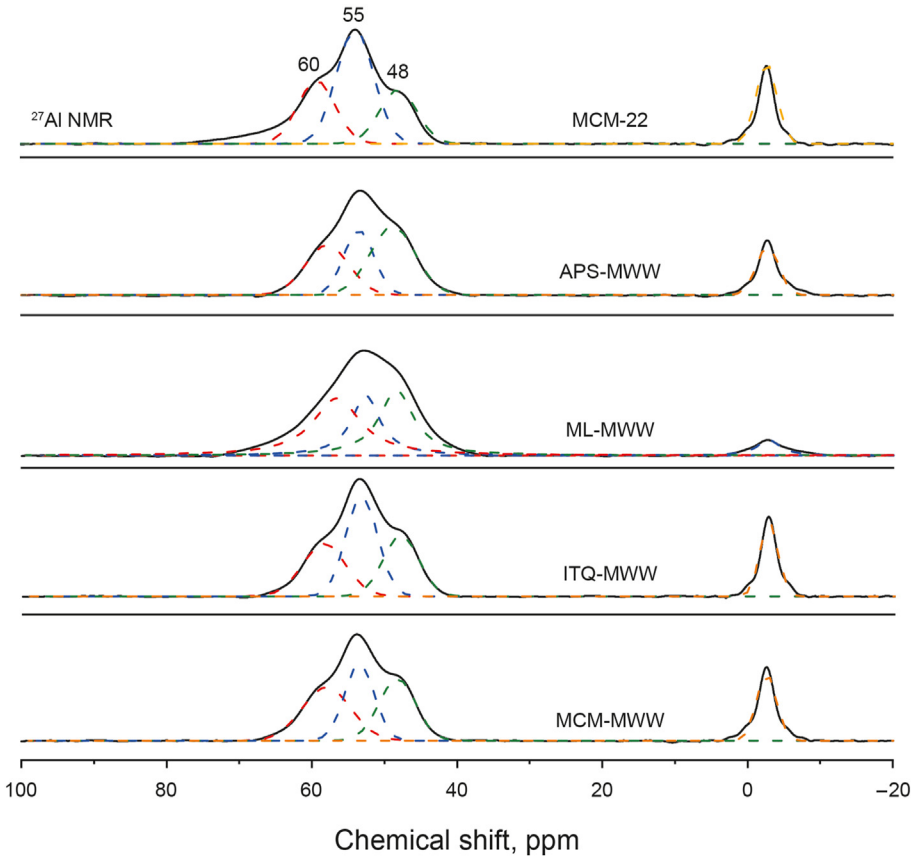

Fig. 6. ^{27}Al MAS NMR spectra of five samples.

3.2. Identifying the APS structural unit and crystallization of APS-MWW

As mentioned, the APS was achieved from the MWW synthetic gel after the aluminosilicate species polymerization before its hydrothermal crystallization. So, what is the APS structure? Why does APS material can boost the rapid growth of MWW crystals? Thus, we further lucubrated the APS structure to explore the essence of rapid crystallization. For APS material, XRD pattern in Fig. 7a gives no characteristic peaks of MWW zeolites between 20° and 26°, showing APS amorphous phase, without existing long range, periodical organization. FT-IR spectra in Fig. 7b shows the characteristic band of 550 cm^{-1}, which is different from the notable feature of the double band (namely a double six rings (D6R), at 555 and 597 cm^{-1} (Corma et al., 1995a, b; Gil et al., 2015)) of MCM-22 zeolite. Raman spectrum in Fig. 7c showed that APS displays the bands at 260 cm^{-1} and 322 cm^{-1} assigned to the bending mode of 6 MR, and the band at 484 cm^{-1} corresponded to the bending vibration of the 4 MR (Yu et al., 2001; Jin et al., 2017). Compared to the initial silica-alumina gel, the intensity of 6 MR bands of APS is higher than that of it (Fig. S4). These results prove that APS can provide a large number of 6 MR units, which may be the basic structural unit for the nucleation of MWW zeolites. SEM images of seeds in Fig. 7d exhibits uniform particles size with 50 nm in diameter. TEM image of APS in Fig. 7e reveals clear bright-to-dark contrast which reflects the existence of mesostructure in interior. The nitrogen sorption isotherms in Fig. 7f gives a typical Langmuir-type curve. The BET surface area of seeds is 226 $m^2\ g^{-1}$, and the micropore volume and the mesopore volume are 0.05 $cm^3\ g^{-1}$ and 0.40 $cm^3\ g^{-1}$, respectively. The above parameters are somewhat consistent with nanosized aluminosilicate materials, but lack of long periodical organization.

To understand the aging process of APS-MWW system, the samples (noted as APS-MWW-P-6h, ML-MWW-P-6h, ITQ-MWW-P-6h, MCM-MWW-P-6h) obtained after the gel aging 6 h at 60 °C were performed by SEM characterization in Fig. S5. The conventional MCM-22 primary particles free of seeds at 6h (Fig. S5a) present amorphous silica with the sizes ranging between 5 and 50 nm. APS-MWW-P-6h sample (Fig. S5b) displays some proportion of amorphous silica and lamella structure. ML-MWW-P-6h (Fig. S5c) also exists visible lamellar structures, which may come from mother liquor. ITQ-MWW-P-6h sample (Fig. S5d) displays some MWW lamellae, which stems from the undissolved MWW fragment of the pure silica ITQ-1 zeolite. For MCM-MWW-P-6h sample (Fig. S5e), more proportion of MCM-22 flakes can be clearly observed, indicating that MCM-22 hardly dissolves during the aging stage, which may be due to the presence of a large amount HMI in MCM-22, thereby stabilizing the zeolite structure (Kamimura et al., 2017). To further illustrate the dissolved state of the seeds in the system, the seeds were treated using the alkalinity solution similar to the synthetic system (Fig. S6). Apparently, the three types of seeds, i.e. APS, ITQ-1, ML (Fig. S6a–c) are almost dissolved or become acicular structure under alkaline conditions, while most of MCM-22 seeds (Fig. S6d) remains the lamella structure in the system, indicating that MCM-22 seeds are relatively stable, and is conducive to the epitaxial growth of lamellar structure.

TPO-MS was employed to further probe the content of the templates in seeds, as shown in Fig. S7. All samples show CO and CO_2 signal peaks. In generally, the peaks at 400–500 °C and

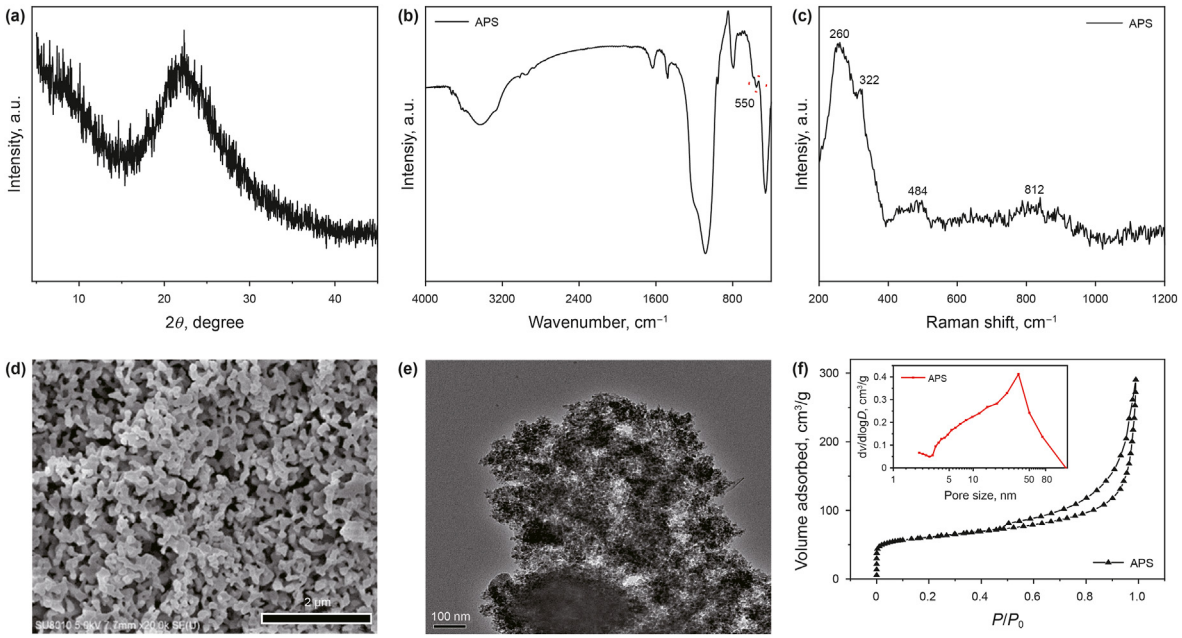

Fig. 7. (**a**) XRD pattern, (**b**) FT-IR spectra, (**c**) Raman spectra, (**d**) SEM image, (**e**) TEM image, (**f**) N_2 adsorption/desorption isotherms and pore-size distribution of APS.

500–700 °C correspond to the loadings of HMI templates in the surface half-cup or supercages and the 10 MR channels, respectively (Jiang et al., 2020; Cao et al., 2021). Obviously, compared with ITQ-1 (peak area is 380) and MCM-22 (peak area is 559), APS (peak area is 25) has the very lowest peak area, which also proves that APS has the lowest templates content. According to previous literature reports, the templates (HMI) has the function of stabilizing the zeolite framework (Díaz et al., 2006; Kamimura et al., 2017). Excessive content of the templates makes the seeds difficult to dissolve, which cannot provide the desired structure units for the zeolite synthesis, thus the minor content of the templates in seeds (i.e. APS seeds) is more likely to produce surface defects, increase the activity of the seeds, and improve the synthesis efficiency. In addition, Kamimura et al. (2017) found that the HMI molecules in the seed remained intact and no significantly change after the synthesis of MWW zeolite. Therefore, in APS synthesis system, it is reasonable speculation that the primary structural unit derived from APS dissolution accelerated the synthesis of MWW zeolites while the presence of HMI had little effect.

The evolution behavior of aluminosilicate species in the synthesis systems during the aging 6 h at 60 °C was investigated by Synchrotron radiation SAXS. As seen in Fig. 8a, the ML, MCM-22 and ITQ-1 systems have very similar SAXS curve shape and they all present "scattering mound" (also called scattering shoulder) in lower q zone, and have larger particle size concentrated at about 10 nm (Fig. 8b). The appearance of scattering shoulder (by Lorentz correction curves (Fig. 8c)) represents the existence of a long-period (L) structure in the system, which is related to the specific size and average distance of the particles in the system (Stribeck, 2007). And heterogeneous particles and spacing may cause low and wide scattering peaks or scattering shoulder. Scattering shoulders of ML-MWW, MCM-MWW and ITQ-MWW systems originate from the incompletely disaggregated tiny lamella structure of seeds, which is consistent with the previous SEM image (Fig. S5). Notably, for APS-MWW, SAXS curve features relative low scatter intensity with nearly lined shape and no scattering shoulder can be observed, which are visibly different from other samples. And APS-MWW sample possesses a wide range of particle size distribution around 2–35 nm (Fig. 8b). In generally, the active species are usually the particles around 2 nm, which is from the depolymerization of the silicon source, and then form larger aluminosilicate species around 10 nm, which are identified as the secondary structural units (Cao et al., 2021). That is to say, the particles are depolymerized and condensed simultaneously, which

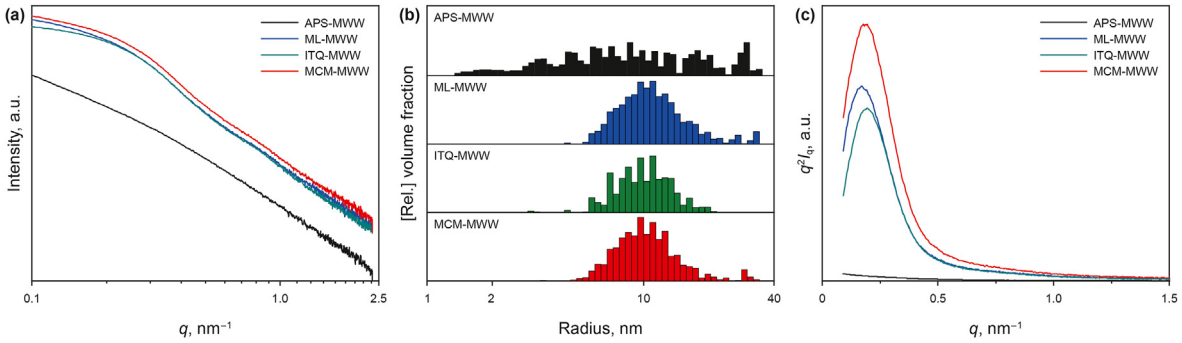

Fig. 8. SAXS patterns of different systems with ageing process for 6 h at 60 °C (**a**) SAXS curves, (**b**) Histogram of the calculated radius size distribution corresponding to the Monte Carlo fits, (**c**) Lorentz correction method.

further demonstrate that the crystallization rate of APS-MWW system is faster than other systems.

After treating the APS and others (ML, MCM-22 and ITQ-1) in the alkalinity solution for 6 h at 60 °C, the samples were obtained and noted as APS-OH, ML-OH, ITQ-1-OH and MCM-22-OH, respectively. As seen in Fig. S8, the periodic structure disappears in the scattering curves for all seeds systems, indicating that the periodic lamella structure seeds have been severely damaged. Combined with SEM images (Fig. S6), the disappearance of the periodic structure is corresponding to the disaggregation of the lamella structure. MCM-22-OH and ITQ-1-OH systems have the large proportion of medium and larger particles with 2–40 nm (Fig. S8b). And small particles of about 2 nm are distributed in the ML-OH system. While larger particles (10–40 nm) are mostly distributed in APS-OH, indicating that different seeds present different aggregation states in the alkaline system.

By powerful SAXS technology, we comparatively studied nucleation and growth processes of zeolite with different crystallization time in APS-MWW and conventional MCM-22 systems (the samples noted as APS-MWW-CX, X represents for crystallization time). The new insight was obtained into the underlying factors that influence crystallization of MWW zeolite by APS. SAXS curve of APS-MWW-C6h sample (Fig. 9a) presented a higher scattering intensity and extensive particle size distribution (R_g = 2–40 nm) (Fig. 9b) (Gommes et al., 2004; Pauw et al., 2013; Bressler et al., 2015). This phenomenon is originated from the polymerization of the active species which came from depolymerization of silicon sources, then to form amorphous aluminosilicate species (also known as secondary structural units). With crystallized time prolonged to 24 h, smaller particles (R_g = 2–10 nm) were gradually reduced and larger particles (R_g = 10–40 nm) were gradually increased at this time, which means that the secondary structural units were gradually consumed to form tertiary structural units (R_g = 10–40 nm). Combined with the crystallization curve (Fig. 2b), the relative crystallinity is rising, indicating that APS-MWW sample is in the crystal growth stage during the period of 6–24 h. While, it takes 36–48 h for MCM-22-C48h sample to form crystals with a similar size as APS-MWW-C6h sample (Fig. S9b). The result indicates that APS-MWW sample takes 6 h to enter the fast growth period, while MCM-22 sample takes 36–72 h enter the crystal growth stage. For MCM-22 system, it takes more than 96 h to form MWW structure. Obviously, the addition of APS promotes the polymerization of silicon and aluminum species to form abundant crystal nucleus which allow a short induction period and fast crystallization of APS-MWW.

The shape of SAXS curves in the q range of 0.1–0.25 nm^{-1} during synthesis process of zeolite are strongly related to an aggregation process between primary units and promotion of zeolite growth. The ln-ln plot analysis of SAXS curves in the crystallization stage of MWW zeolite presents the existence of linear regions, which can be related to the fractal structure of the resulting aggregates (Zhao et al., 2017). Fig. 9c shows the fractal analysis of APS-MWW system with the crystallization time and the corresponding fractal dimensions are listed in Table S5. In the induction period (before 6 h and 12 h), the species in APS-MWW mixtures (including primary particles and partly APS) displays mass fractal (D_m = 2.57, 2.67). Then, the primary units through successive secondary aggregation form larger secondary structural units. During the crystal growth period from 12 to 24 h, APS-MWW samples demonstrate surface fractal (D_s = 2.08, 2.00), the secondary structural units transform into the spherical particles and the particles have smoother surface in line with the SEM images. At the growth stable period (36–48 h), samples exist mass fractal (D_m = 2.18, 1.75), thus, the lamellar structure completely forms on the surface of the spherical particles. The D_m is closer to 2, indicative of two-dimensional objects (Schmidt, 1991), such as flake-like shape as seen in the SEM images. The synthesis of APS-MWW experiences three stages, nucleation to growth and then to the stable period, corresponding with transformation from mass fractal to surface fractal, and to mass fractal, resulting in a loose two-dimensional lamellar structure.

Differently, the conventional MCM-22 synthesis process (Fig. S9c and Table S5), experiences slow growth process along with transformation from surface fractal to mass fractal, and surface fractal first decreases and then increases. This phenomenon stems from the slow depolymerization of the silicon source during the induction period. Clearly, at the end of the induction period (at 48 h), the particle D_s is 2.01, indicative of aggregate with smooth surface as seen in SEM image. During the 48–72 h, the surface of the aggregates begins to form a lamellar structure with rougher surface (D_s = 2.77). After 96 h, the surface fractal transforms to mass fractal, indicating the formation of a two-dimensional lamellar structure, which is similar to APS-MWW systems. The fractal results provide an important guiding significance for the particle density and morphology, and it also affords a completely new visual angle for understanding the crystallization of MWW zeolites.

FT-IR was used to further investigate the growth process of APS-MWW, as shown in Fig. 10. The bands at 2936 cm^{-1}, 2862 cm^{-1} and 1465 cm^{-1} belong to the C–H stretching vibration of HMI molecule (Corma et al., 1995a, b; Gil et al., 2015), when the crystallization time is 0 h, there is a weak C–H stretching vibration band, indicating that there is a small amount of HMI molecules in seeds;

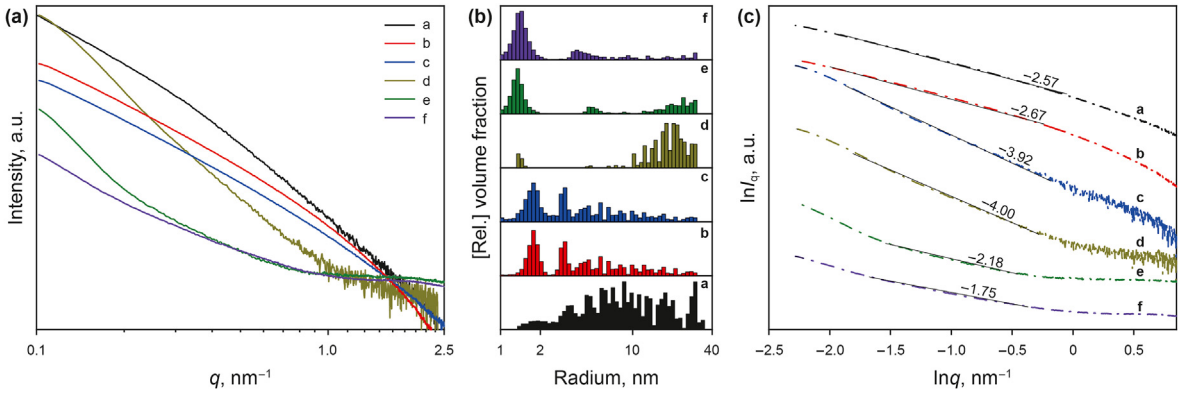

Fig. 9. APS-MWW sample with different crystallization stage (**a**) scattering curves, (**b**) Monte Carlo fits to the measured SAXS intensity profiles, (**c**) fractal dimension, (a-6 h, b-12 h, c-18 h, d-24 h, e-36 h, f-48 h).

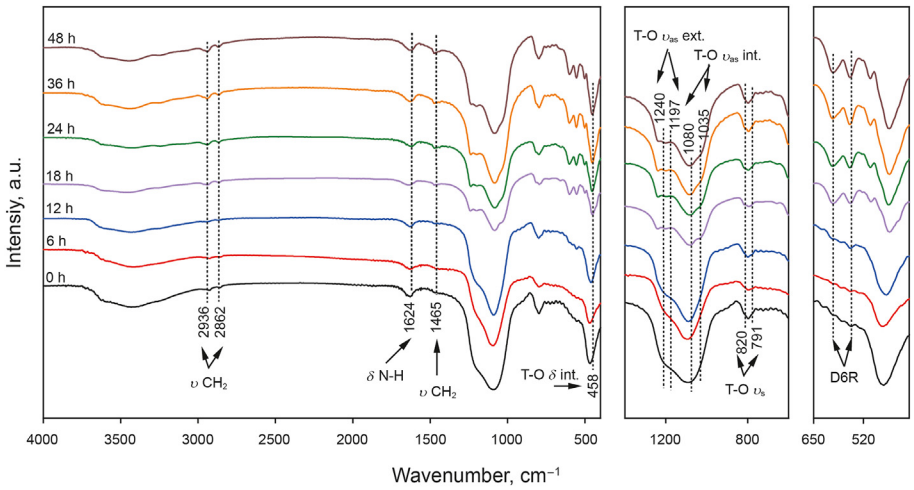

Fig. 10. FT-IR spectra of the APS-MWW synthesis system at different times.

when the crystallization time was prolonged from 0 to 18 h, the band intensity gradually increased, and when the crystallization time reached 18 h, the band intensity is not changing, indicating that the evolution of HMI molecule between flakes mainly occurred before 18 h. In addition, the D6R (Fig. 10) is the characteristic structure of MWW zeolite (Corma et al., 1995a, b; Gil et al., 2015), there is a weak signal bands at 0 h, indicating that the crystal has begun to grow during the aging process in the APS system. The addition of APS significantly shortens the induction period and growth period during zeolite synthesis. With the extension of crystallization time, the band intensity gradually increased, indicating that the number of D6R structures increased and the crystallization was gradually completed. In addition, the framework vibration of MWW zeolite were observed, as shown in Fig. 10, mainly including the asymmetric stretching vibration of T-O (T-O υ_{as} ext.) at 1240 cm^{-1} and 1197 cm^{-1}, the T-O internal symmetric stretching vibrations (T-O υ_{as} int.)) at 1080 cm^{-1} and 1035 cm^{-1}, the T-O tetrahedra internal symmetric stretching vibrations (T-O υ_s) at 820 cm^{-1} and 791 cm^{-1}, and the T-O bending vibration (T-O δ int.) at 458 cm^{-1} (Gil et al., 2015; Cao et al., 2021). The intensities of these bands gradually increased, reflecting the growing process of MWW zeolite.

The synthesis parameters coupled with literature work are listed in Table S6, which highlights the influence of seeds on the synthesis MWW zeolite, including the recipe and crystallization conditions (Díaz et al., 2006; Shi et al., 2015; Kamimura et al., 2017; Rodrigues et al., 2018). Surprisingly, the APS-assisted synthesis allows the lowest HMI/SiO_2 ratio, NaOH/SiO_2 ratio, H_2O/SiO_2 ratio, and the shortest crystallization time, among the literature results.

3.3. Crystallization mechanism of MWW zeolite

Fig. 11 shows the crystallization behavior of different MWW synthesis systems. SAXS, Raman and FT-IR analysis results show that APS can provide a large number of 6 MR structural units (primary structural unit) in the ageing stage (path A), to improve crystal nucleation and the APS-MWW zeolite growth. While for other three seeds (path B), ML, ITQ-1 and MCM-22 seeds, formation of crystal nuclei requires more time to depolymerize the seed crystals, thus a few primary structural units appear in ageing stage. The conventional MCM-22 system (path C) only possesses abundant aluminosilicates and few nucleus particles. Specifically, adopting the APS, the dissolution/condensation of the aluminosilicate and/or silicate species in a short induction time (12 h) can form a large number of secondary and tertiary structural units, leading to a large number of crystal nucleus. However, the other seed systems (ITQ-MWW, ML-MWW, and MCM-MWW) need more than 18 h, the seed-free MCM-22 system even takes 36 h. In the growth period, due to presence of a large number of crystal nuclei, APS-MWW mixtures rapidly grew into a smaller and thinner MWW hexagonal nanosheets, therein the crystal flakes reduced to a size of 200–400 nm with a thickness of 5–20 nm. While the ITQ-1 and MCM-22 seeds retain partly fragmentized MWW sheets, which benefit to epitaxial growth of ITQ-MWW and MCM-MWW, resulting in the generation of a larger size layers samples. There are microcrystalline particles (MWW fragment) in ML to promote the nucleation of MWW, and finally form a thinner and smaller MWW layers. For seed-free MCM-22 system, only single HMI generates the nucleation and growth of MWW crystals during the whole synthesis stage, and thus it forms more and more dispersed lamellar structure.

3.4. Acid properties and catalytic performance

NH_3-TPD profiles (Fig. S10) of all the H-types samples have two obvious signal peaks in the temperature regions 100–350 °C and 350–600 °C, which are assigned to weak (W) and strong (S) acid sites, respectively. The conventional MCM-22 sample (0.88 mmol g^{-1}, Table 2) has the biggest acid concentration among all seed-assisted samples, while the total acid content of APS-MWW system (0.79 mmol g^{-1}) is close to MCM-22. APS-MWW (0.48 mmol g^{-1}) and MCM-22 (0.50 mmol g^{-1}) has more strong acid sites, which may be utilized in the benzene alkylation reaction. Notably, the S/W ratio of APS-MWW is higher than that of conventional MCM-22 sample. As reported (Díaz et al., 2006), a lower HMI/SiO_2 ratio cause defects in the connection of the MWW layer, leading to a larger external surface area, thus provide more active centers on the external surface, which may improve the catalytic reaction that occurs on the outer surface of the catalyst. Py-IR spectroscopy offers the amounts of total and strong acid sites at 200 °C and 350 °C, respectively (Fig. S11). The amounts of Brønsted acid sites (BAS or B) and Lewis acid sites (LAS or L) for each sample are given in Table 2. The amounts of BAS reduce in the following sequence: MCM-22 > APS-MWW > ITQ-MWW > ML-MWW > MCM-MWW. The samples with larger S/W ratio and more BAS content could facilitate increasing the activity of the alkylation reaction. In addition, the 2,6-di-tert-butylpyridine (DTBP) larger than the 10 MR was used to be a probe to detect BAS on the external

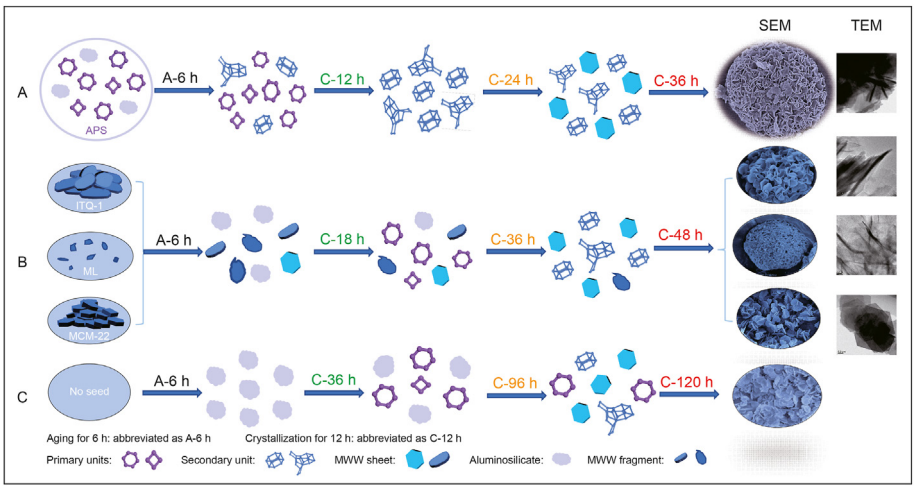

Fig. 11. The promotive role of active precursor APS in the crystallization of MWW zeolite.

Table 2
Acid properties of five samples.

Samples	NH_3-TPD			Py-IR				
	Acid amount, mmol g^{-1}			200 °C, mmol g^{-1}		350 °C, mmol g^{-1}		
	W[a]	S[a]	S/W[a]	BAS[b]	LAS[b]	BAS[b]	LAS[b]	B/L[b]
MCM-22	0.38	0.50	1.32	0.361	0.392	0.335	0.145	2.31
APS-MWW	0.31	0.48	1.54	0.342	0.416	0.332	0.137	2.42
ML-MWW	0.28	0.42	1.50	0.351	0.402	0.312	0.131	2.38
ITQ-MWW	0.26	0.38	1.46	0.363	0.451	0.327	0.139	2.35
MCM-MWW	0.33	0.44	1.33	0.284	0.316	0.231	0.110	2.10

[a] W, S and S/W stand for Weak acid, Strong acid and Strong/Weak ratio.
[b] BAS, LAS and B/L stand for Brønsted acid sites, Lewis acid sites and Brønsted/Lewis acid ratio, respectively.

pockets of MWW zeolites. The band considered at 3365 cm^{-1} is corresponded to the protonated DTBP (Fig. S12 and Table S7) (Margarit et al., 2015; Jiang et al., 2020). Compared with traditional MCM-22 zeolite, when DTBP is used as an adsorbed probe, the accessible BAS concentration in APS-MWW and ML-MWWW is nearly twice that of it.

1,3,5-triisopropylbenzene (TIPB) cracking reaction was used to further demonstrate the BAS on the external surfaces, due to its diffusion strongly impeded in 10 MR channels of MCM-22, which mainly react with the acid sites located at the external surface of MWW zeolites (Margarit et al., 2015). The results of TIPB cracking reaction are presented in Fig. S13. Initial conversion decreases in the order of APS-MWW (92.4%) > ML-MWW (90.2%) > ITQ-MWW (85.6%) > MCM-22 (82.5%) > MCM-MWW (80.1%), which is consistent with the results of BAS on the external surface. The conversion rate of APS-MWW and ML-MWW is higher than that of MCM-22, which can provide more active sites for macromolecular reactions.

All samples were evaluated in the reaction of benzene-ethylene liquid phase alkylation as shown in Table S8 and Figs. 12 and S14. The APS-MWW, MCM-MWW and MCM-22 catalysts reveal a higher benzene conversion, basically remaining between 30% and 32%. The ethylbenzene selectivity over the ITQ-MWW zeolite is the highest (over 90%), while other types of MWW catalyst lay between 87% and 89%. Furthermore, APS-MWW has the highest yields (28.03%) among these five catalysts. Probably due to the APS-MWW catalyst with smaller size, featuring higher external specific surface area

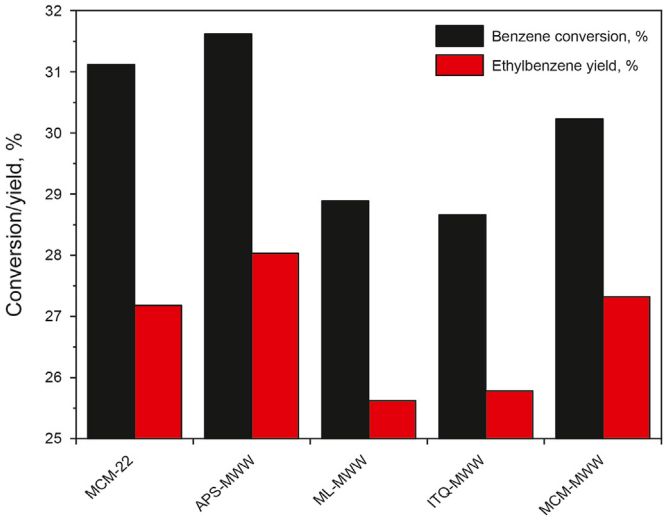

Fig. 12. Benzene conversion and ethylbenzene yield of five MWW zeolites. ($T = 210$ °C, $P = 3.0$ MPa, WHSV (ethylene) = 1 h^{-1}, benzene/ethylene (mol·mol^{-1}) = 2.6).

and larger mesopore volume gives an out-bound performance in the liquid phase alkylation. Ultimately, adopting APS assisted synthesis approves an extensive application prospect in the alkylation reaction for industrial applications.

4. Conclusion

We present a simple and efficient route to prepare MWW zeolite by introducing specific structure of APS. For understanding the role of APS, synthesis of MCM-22 zeolites by adding the APS was compared with other types of seeds in the MCM-22 synthetic mixture, i.e. ML, ITQ-1 and MCM-22, respectively. The seeds significantly influence the lamellar morphology of MWW zeolite and synthesis efficiency. Adopting APS proves rapid crystallization of APS-MWW within 36 h, while it would take 120 h to form the conventional MCM-22 zeolite. APS-MWW sample presents a smaller and thinner layer structure, with the crystal flakes of 200–400 nm in size and 5–20 nm in thickness, while MCM-MWW and ITQ-MWW possesses a larger crystal flakes size (about 500 nm)

in comparison with MCM-22 sample. Meanwhile, ML-MWW and ITQ-MWW thicknesses are about 2.5–10 nm and 5–15 nm, respectively. The effect of different types of seeds in the ageing process to accelerate formation of MCM-22 zeolite was revealed. Notably, the APS material is more active to improve crystal nucleation and APS-MWW zeolite growth, because it provides a large number of 6 MR structural units. Compared with conventional MCM-22 catalyst, the APS-assisted MWW zeolite presents well-crystallized structure with higher mesoporous volume and more strong BAS, due to its thinner lamella morphology, rendering more active sites in the available channels. Finally, APS-MWW zeolite performs the high catalytic activity, selectivity, and stability in the reaction of benzene-ethylene liquid phase alkylation. This work adequately testifies that the potential applications of APS-assisted synthesis MWW zeolites in catalytic field. The efficient preparation of MWW zeolites has laid a solid foundation for the further development of petrochemical industry.

Acknowledgments

This work was supported by the National Natural Science Foundation of China (22078356, U1662116, U1910206). The authors thank the Foundation of State Key Laboratory of Coal Conversion (J21-22-604) and PetroChina research institute of petroleum processing program (PRIKY20065).

Appendix A. Supplementary data

Supplementary data to this article can be found online at https://doi.org/10.1016/j.petsci.2023.01.005.

References

Aguilar, J., Pergher, S.B.C., Detoni, C., et al., 2008. Alkylation of biphenyl with propylene using MCM-22 and ITQ-2 zeolites. Catal. Today 133, 667–672. https://doi.org/10.1016/j.cattod.2007.11.057.

Bressler, I., Pauw, B.R., Thünemann, A.F., 2015. McSAS: software for the retrieval of model parameter distributions from scattering patterns. J. Appl. Crystallogr. 48, 962–969. https://doi.org/10.1107/S1600576715007347.

Bai, R., Navarro, M.T., Song, Y., et al., 2020. Titanosilicate zeolite precursors for highly efficient oxidation reactions. Chem. Sci. 11, 12341–12349. https://doi.org/10.1039/D0SC04603E.

Corma, A., Corell, C., Fornés, V., 1995a. Infrared spectroscopy thermoprogrammed desorption and nuclear magnetic resonance study of the acidity structure and stability of zeolite MCM-22. Zeolites 15, 576–582. https://doi.org/10.1016/0144-2449(95)00015-X.

Corma, A., Corell, C., Pérez-Pariente, J., 1995b. Synthesis and characterization of the MCM-22 zeolite. Zeolites 15, 2–8. https://doi.org/10.1016/0144-2449(94)00013-I.

Corma, A., Corell, C., Pérez-Pariente, J., et al., 1996. Adsorption and catalytic properties of MCM-22: the influence of zeolite structure. Zeolites 16, 7–14. https://doi.org/10.1016/0144-2449(95)00084-4.

Corma, A., Diaz, U., Fornés, V., et al., 2000a. Characterization and catalytic activity of MCM-22 and MCM-56 compared with ITQ-2. J. Catal. 191 (1), 218–224. https://doi.org/10.1006/jcat.1999.2774.

Corma, A., Fornés, V., Guil, J.M., et al., 2000b. Preparation, characterisation and catalytic activity of ITQ-2, a delaminated zeolite. Microporous Mesoporous Mater. 38 (2–3), 301–309. https://doi.org/10.1016/S1387-1811(00)00149-9.

Corma, A., Martínez-Soria, V., Schnoeveld, E., 2000c. Alkylation of benzene with short-chain olefins over MCM-22 zeolite: catalytic behaviour and kinetic mechanism. J. Catal. 192 (1), 163–173. https://doi.org/10.1006/jcat.2000.2849.

Carriço, C.S., Cruz, F.T., dos Santos, M.B., 2016. MWW-types catalysts for gas phase glycerol dehydration to acrolein. J. Catal. 334, 34–41. https://doi.org/10.1016/j.jcat.2015.11.010.

Cao, S.W., Shang, Y.S., Liu, Y.S., et al., 2021. Desert rose" MCM-22 microsphere: synthesis formation mechanism and alkylation performance. Microporous Mesoporous Mater. 315, 110910. https://doi.org/10.1016/j.micromeso.2021.110910.

Du, H.W., Olson, D.H., 2002. Surface acidic properties of A HMCM-22 zeolite: collidine poisoning and hydrocarbon adsorption studies. J. Phys. Chem. B 106 (2), 395–400. https://doi.org/10.1021/jp013310s.

Díaz, U., Fornés, V., Corma, A., 2006. On the mechanism of zeolite growing: crystallization by seeding with delayered zeolites. Microporous Mesoporous Mater. 90 (1–3), 73–80. https://doi.org/10.1016/j.micromeso.2005.09.025.

Ebrahimi, A.N., Sharak, A.Z., Mousavi, S.A., et al., 2011. Modification and optimization of benzene alkylation process for production of ethylbenzene. Chem. Eng. Process 50 (1), 31–36. https://doi.org/10.1016/j.cep.2010.10.011.

Fan, W., Ogura, M., Sankar, G., et al., 2007. In situ Small-angle and wide-angle X-ray scattering investigation on nucleation and crystal growth of nanosized zeolite. A. Chem. Mater. 19, 1906–1917. https://doi.org/10.1021/cm062827j.

Gommes, C., Blacher, S., Goderis, B., et al., 2004. In situ SAXS analysis of silica gel formation with an additive. J. Phys. Chem. B 108, 8983–8991. https://doi.org/10.1021/jp049568a.

Gil, B., Roth, W.J., Makowshi, W., et al., 2015. Facile evaluation of the crystallization and quality of the transient layered zeolite MCM-56 by infrared spectroscopy. Catal. Today 243, 39–45. https://doi.org/10.1016/j.cattod.2014.07.031.

Hould, N.D., Lobo, R.F., 2008. Nanoparticle Precursors and phase selectivity in hydrothermal synthesis of zeolite β. Chem. Mater. 20, 5807–5815. https://doi.org/10.1021/cm800884q.

Hould, N.D., Kumar, S., Tsapatsis, M., et al., 2010. Structure and colloidal stability of nanosized zeolite beta precursors. Langmuir 26 (2), 1260–1270. https://doi.org/10.1021/la902445c.

Hould, N.D., Foster, A., Lobo, R.F., 2011. Zeolite beta mechanisms of nucleation and growth. Microporous Mesoporous Mater. 142, 104–115. https://doi.org/10.1016/j.micromeso.2010.11.024.

Haw, K.G., Gilson, J.P., Nesterenko, N., et al., 2018. Supported embryonic zeolites and their use to process bulky molecules. ACS Catal. 8, 8199–8212. https://doi.org/10.1021/acscatal.8b01936.

Inagaki, S., Thomas, K., Ruaux, V., et al., 2014. Crystal growth kinetics as a tool for controlling the catalytic performance of a FAU-types basic catalyst. ACS Catal. 4, 2333–2341. https://doi.org/10.1021/cs500153e.

Jin, S., Wang, Z., Tao, G., et al., 2017. UV resonance Raman spectroscopic insight into titanium species and structure-performance relationship in boron-free Ti-MWW zeolite. J. Catal. 353, 305–314. https://doi.org/10.1016/j.jcat.2017.07.032.

Jiang, L., Li, X.Y., Gong, Y.J., et al., 2020. MCM-56 stabilization synthesis using auxiliary tetraethylammounium ions: its role to inhibit surface Si-O-Al bridged linkage and retain highly delaminated structure. Microporous Mesoporous Mater. 302, 110245. https://doi.org/10.1016/j.micromeso.2020.110245.

Khlebnikova, E., Ivashkina, E., Dolganova, I., 2017. Benzene alkylation with ethylene: the way to increase the process efficiency. Chem. Eng. Process 120, 234–240. https://doi.org/10.1016/j.cep.2017.07.002.

Kamimura, Y., Itabashi, K., Kon, Y., 2017. Seed-assisted synthesis of MWW-types zeolite with organic structure-directing agent-free Na-aluminosilicate gel system. Chem. Asian J. 12, 530–542. https://doi.org/10.1002/asia.201601569.

Liu, K., Xie, S., Liu, S., et al., 2011. Catalytic role of different pore systems in MCM-49 zeolite for liquid alkylation of benzene with ethylene. J. Catal. 283 (1), 68–74. https://doi.org/10.1016/j.jcat.2011.07.004.

Luo, H.Y., Michaelis, V.K., Hodges, S., et al., 2015. One-pot synthesis of MWW zeolite nanosheets using a rationally designed organic structure-directing agent. Chem. Sci. 6 (11), 6320–6324. https://doi.org/10.1039/C5SC01912E.

Maheshwari, S., Martínez, C., Portilla, M.T., et al., 2010. Influence of layer structure preservation on the catalytic properties of the pillared zeolite MCM-36. J. Catal. 272 (2), 298–308. https://doi.org/10.1016/j.jcat.2010.04.011.

Margarit, V.J., Martínez-Armero, M.E., Navarro, M.T., et al., 2015. Direct dual-template synthesis of MWW zeolite monolayers. Angew. Chem. Int. Ed. 127, 13928–13932. https://doi.org/10.1002/anie.201506822.

Pauw, B.R., Pedersen, J.S., Tardif, S., et al., 2013. Improvements and considerations for size distribution retrieval from small-angle scattering data by Monte Carlo methods. J. Appl. Crystallogr. 46, 365–371. https://doi.org/10.1107/S0021889813001295.

Rodrigues, M.V., Vieira, L.H., Campos, G.P., et al., 2018. Effect of different seed sources on the hydrothermal crystallization of MCM-22 zeolite catalysts. CrystEngComm 20, 3467–3475. https://doi.org/10.1039/C8CE00448J.

Schmidt, P.W., 1991. Small-angle scattering studies of disordered porous and fractal systems. J. Appl. Crystallogr. 24, 414–435. https://doi.org/10.1107/S0021889891003400.

Stribeck, N., 2007. X-Ray Scattering of Soft Matter. Springer Laboratory, Berli. Springer Berlin Heidelberg. https://doi.org/10.1007/978-3-540-69856-2.

Shi, Y., Xing, E., Xie, W., et al., 2015. Directing gel: an effective method tailoring morphology of MWW zeolites and their catalytic performance in liquid-phase alkylation of benzene with ethylene. Microporous Mesoporous Mater. 215, 8–19. https://doi.org/10.1016/j.micromeso.2015.04.041.

Schwanke, A.J., Vinaches, P., Meneau, F., et al., 2020. Nucleation and crystallization of the MWW-types lamellar zeolitic precursor. Catal. Today 344, 102–107. https://doi.org/10.1016/j.cattod.2018.10.033.

Sheng, Z., Li, H., Du, K., et al., 2021. Observing a zeolite nucleus (subcrystal) with a uniform framework structure and its oriented attachment without single-molecule addition. Angew. Chem. 60, 13444–13451. https://doi.org/10.1002/ange.202102621.

Tompsett, G.A., Panzarella, B.A., Conner, W.C., et al., 2007. In situ SAXS and WAXS of zeolite microwave synthesis. Nucl. Instrum. Methods Phys. Res. Sect. B Beam Interact. Mater. Atoms 261, 863–866. https://doi.org/10.1016/j.nimb.2007.04.224.

Wang, L., Zhu, D., Wang, J., et al., 2021. Embryonic zeolite-assisted synthesis of SSZ-13 with superior efficiency and their excellent catalytic performance. J. Mater. Chem. A. 9, 15238–15245. https://doi.org/10.1039/D1TA01452H.

Yu, Y., Xiong, G., Li, C., et al., 2001. Characterization of aluminosilicate zeolites by UV Raman spectroscopy. Microporous Mesoporous Mater. 46, 23–34. https://doi.org/10.1016/S1387-1811(01)00271-2.

Yang, W., Wang, Z., Sun, H., et al., 2016. Advances in development and industrial applications of ethylbenzene processes. Chin. J. Catal. 37 (1), 16–26. https://doi.org/10.1016/S1872-2067(15)60965-2.

Zhang, B., Ji, Y., Wang, Z., et al., 2012. Liquid-phase alkylation of benzene with ethylene over post-synthesized MCM-56 analogues. Appl. Catal., A 443 (7), 103–110. https://doi.org/10.1016/j.apcata.2012.07.028.

Zhao, X., Liu, R., Zhang, H., et al., 2017. Structure evolution of aluminosilicate sol and its structure-directing effect on the synthesis of NaY zeolite. J. Appl. Crystallogr. 50, 231–239. https://doi.org/10.1107/S1600576716020409.